Article | Open Access

Energy Materials

Du *et al. Energy Mater.* **2026**, *6*, 600098 **DOI:**10.20517/energymater.2026.101

Molecular engineering of coffee grounds via exogenous precursor-guided hydrothermal carbonization and activation for high-performance supercapacitor electrodes

Yuhan Du#, Yulu Yang#, Peigao Duan*

Keywords:
Coffee ground, hydrothermal carbonization, activation, heteroatom doping, porous carbons, supercapacitor

Citation: Du, Y.; Yang, Y.; Duan, P. Molecular engineering of coffee grounds via exogenous precursor-guided hydrothermal carbonization and activation for high-performance supercapacitor electrodes. *Energy Mater.* **2026**, *6*, 600098. https://dx.doi.org/10.20517/energymater.2026.101

Received: 30 Apr 2026
First Decision: 3 Jun 2026
Revised: 29 Jun 2026
Accepted: 10 Jul 2026
Published: 11 Aug 2026

Academic Editors:
Heng Zhang, Yuping Wu
Copy Editor:
Ping Zhang
Production Editor:
Ping Zhang

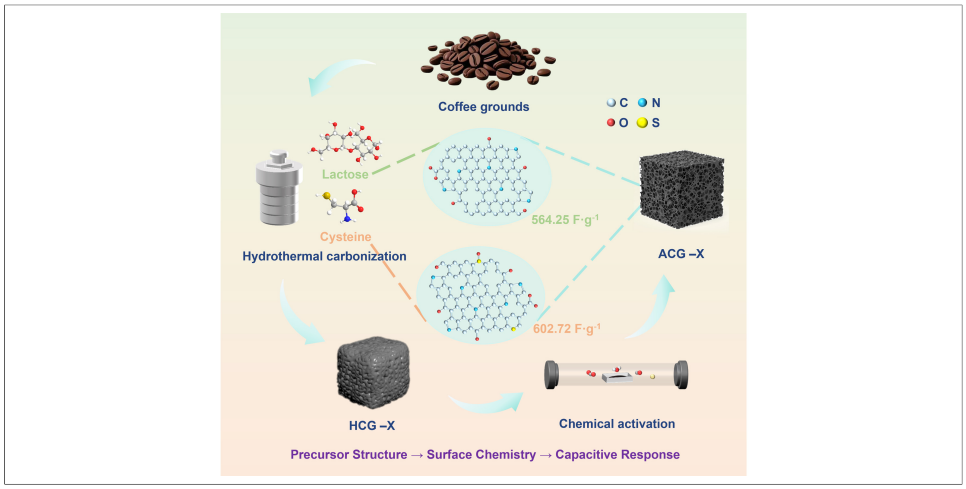

Abstract

Biomass-derived porous carbons are promising electrode materials, but their surface chemistry is often limited by the inherent heteroatoms of the feedstock, restricting their tunability and high-level performance. This study introduces a precursor-guided chemical engineering strategy to actively regulate the surface chemistry and pore structure of ground-derived porous carbon. By incorporating various exogenous sugar (glucose, fructose, xylose, lactose, and sucrose) and amino acid (lysine, glycine, cysteine, glutamic acid, and proline) precursors during hydrothermal precarbonization, followed by KOH activation, we systematically investigated the relationship between the precursor molecular structure and the final carbon properties. A trade-off between "chemical gain" from heteroatom doping and "physical loss" in porosity was identified and discussed. Among the sugar precursors, lactose demonstrated the optimal balance, retaining moderate porosity while achieving a high N/O content (7.64 at%) for a capacitance of 564.25 F·g^{-1}. Notably, a cysteine-an amino acid precursor enabled superior "chemical gain" via N/O/S triple-doping (N + O + S = 7.68 at%), with a high concentration of

State Key Laboratory of Fluorine & Nitrogen Chemicals, School of Chemical Engineering and Technology, Xi'an Jiaotong University, Xi'an 710049, Shaanxi, China.
#Authors contributed equally.

***Correspondence to:** Dr. Peigao Duan, State Key Laboratory of Fluorine & Nitrogen Chemicals, School of Chemical Engineering and Technology, Xi'an Jiaotong University, Xi'an 710049, Shaanxi, China. E-mail: pgduan@xjtu.edu.cn

pseudocapacitive sites (N-5: 60.20%, C=O: 2.21 at%, and sulfur) that effectively compensated for its moderate specific surface area (1,920.91 $m^2 \cdot g^{-1}$). This cysteine-derived carbon delivered the highest specific capacitance of 602.72 $F \cdot g^{-1}$ at 0.5 $A \cdot g^{-1}$ in a three-electrode system. A symmetric supercapacitor based on this material exhibited a competitive energy density of 17.89 $Wh \cdot kg^{-1}$. This work establishes a clear "precursor structure → surface chemistry → capacitive response" paradigm, demonstrating that strategic molecular engineering can unlock high-performance supercapacitor electrodes from lignocellulosic waste.

INTRODUCTION

Supercapacitors are widely recognized as promising energy storage devices for renewable power systems, electric vehicles, and portable electronics because of their high power density, fast charge-discharge rates, and outstanding long-term stability[1,2]. Electrode materials are central to device performance, and biomass-derived porous carbons have emerged as among the most promising candidates because of their wide availability, low cost, environmental friendliness, and inherently rich oxygen functional groups and hierarchical pore structures[3-6]. Among the various biomass precursors, spent coffee grounds are particularly attractive because of their high carbon yield, low ash content, and naturally abundant nitrogen species[7-9]. Our previous work demonstrated that a hydrothermal-activation synergy strategy can convert coffee grounds into N/O-codoped hierarchical porous carbon, with the resulting material delivering a specific capacitance of 546.08 $F \cdot g^{-1}$ at 0.5 $A \cdot g^{-1}$. However, the heteroatom doping in this process relies primarily on the in situ pyrolytic conversion of proteins and polysaccharides inherent to the coffee grounds, meaning that the doping type, content, and configuration are constrained by the intrinsic composition of the raw material, leaving limited room for tuning the surface chemistry.

Strategies for enhancing the electrochemical performance of biomass-derived carbons can be broadly divided into pore structure engineering and surface chemistry regulation[10-12]. Pore structure engineering strategies-such as KOH etching[13], steam treatment[14], CO_2 activation[15], and molten-salt-assisted synthesis[16]-have been extensively used to create hierarchical porous architectures that promote ion diffusion and charge accumulation via high specific surface areas and tailored pore size distributions. In terms of surface chemistry, heteroatom doping with N, O, S, P, and other elements has been demonstrated to improve capacitance performance through pseudocapacitive contributions, enhanced electrolyte wettability, and improved electrical conductivity[17-19]. However, existing heteroatom doping approaches still rely predominantly on the pyrolytic retention of inherent biomass components or posttreatment impregnation. The former is limited by feedstock composition, whereas the latter suffers from poor doping uniformity and low thermal stability of the introduced functional groups. Achieving deliberate design of surface chemistry while maintaining a favorable pore structure remains a central challenge in this field.

More recently, hydrothermal carbonization assisted by exogenous small-molecule precursors has attracted increasing attention as a versatile approach for surface chemistry engineering[20,21]. Unlike conventional posttreatment doping, this approach introduces small molecules bearing specific functional groups during the hydrothermal stage, enabling molecular-level control over carbon framework construction and heteroatom anchoring. Sugars and amino acids are two representative classes of exogenous precursors. The carbon chain length, degree of polymerization, and reducing character of sugars can significantly influence dehydration-polycondensation kinetics and the degree of precursor densification[22-25], whereas the side-chain functional groups of amino acids directly govern crosslinking modes, steric hindrance, and the retention efficiency and configuration of N/O/S heteroatoms[26-28]. Introducing reducing sugars into biomass hydrothermal systems promotes the chemical anchoring of nitrogenous structures through carbonyl-amine (Maillard) reactions[29,30], and sulfur-containing amino acids enable in situ sulfur doping with enhanced electrochemical performance[31]. However, existing studies have largely focused on single precursor types or

individual performance metrics, and a systematic comparison of different precursor molecular structures is lacking. The complete structure-property relationship-"precursor molecular structure → polycondensation/carbonization pathway → surface chemical composition and configuration → capacitive response"-remains poorly understood. More critically, exogenous precursors that enhance surface chemistry often simultaneously promote polycondensation-induced densification, leading to reduced specific surface area and pore volume. How to balance "surface chemistry gain" against "physical charge storage loss" and the mechanisms and limits thereof have yet to be elucidated.

To address these issues, this study builds on our previously optimized hydrothermal-activation process and selects five sugars (glucose, fructose, xylose, lactose, and sucrose) and five amino acids (lysine, glycine, cysteine, glutamic acid, and proline) as exogenous precursors. We systematically investigate how their molecular structures regulate the pore evolution, carbon framework ordering, heteroatom doping configuration, and electrochemical performance of ground-derived porous carbon. This study focuses on three key questions: (1) How do the carbon chain length, degree of polymerization, and reducing characteristics of sugars synergistically govern the polycondensation behavior and carbon framework characteristics? (2) How do the steric hindrance and functional group types of amino acid side chains direct the surface chemical composition and active site distribution? (3) Under conditions of substantially reduced specific surface area, can surface chemistry optimization compensate for physical charge storage loss through enhanced pseudocapacitance-that is, what are the conditions and limits of the "chemical gain" mechanism? By elucidating the structure-property relationship linking the precursor configuration, polycondensation/carbonization pathway, surface chemistry, and capacitive response, this work aims to provide theoretical guidance and practical insights for the targeted design of surface chemistry in high-performance biomass-derived porous carbon electrodes.

EXPERIMENTAL

Materials

In this study, coffee grounds (CG) procured from Saturnbird Coffee Company (Changsha, China) were oven-dried at 105 °C for 12 h to achieve a constant weight. All sugars (glucose, fructose, xylose, lactose, and sucrose, 99%) and amino acids (glycine, L-glutamic acid, L-proline, L-cysteine, and L-lysine hydrochloride, 99%) were purchased from Shanghai Macklin Biochemical Co., Ltd. All other chemical reagents, including hydrochloric acid (HCl, 37%), potassium hydroxide (KOH, ≥ 85%), and polytetrafluoroethylene (PTFE, 60% dispersion), were analytical grade products from Sinopharm Chemical Reagent Co., Ltd., and were used as received without further purification. The raw materials were processed under ambient laboratory conditions (25 ± 2 °C, 45 ± 5% relative humidity) prior to experimental treatments.

Preparation of exogenous precursor-regulated coffee ground-derived porous carbons

Five grams of dried coffee grounds, 50 mL of deionized water, and an exogenous precursor (sugar or amino acid) were sealed in a 100 mL autoclave (Nanjing Zhengxin Instrument Co., Ltd., China) and heated to 280 °C for 30 min under mechanical stirring. The concentration of each precursor was fixed at 0.10 mol·L^{-1}, corresponding to the following masses: 0.90 g (glucose), 0.90 g (fructose), 1.71 g (lactose), 0.75 g (xylose), 1.71 g (sucrose), 0.38 g (glycine), 0.74 g (L-glutamic acid), 0.58 g (L-proline), 0.61 g (L-cysteine), and 0.91 g (L-lysine hydrochloride). Comparisons in this work were conducted on the basis of equal molar concentrations to ensure comparable precursor concentrations and a consistent reactive environment during hydrothermal polycondensations and heteroatom incorporation. The resulting hydrochar was collected by filtration, washed, and dried at 105 °C for 12 h. The sugar-derived hydrochars were labeled HC-X (X = Glu, Fru, Xyl, Lac, and Suc for glucose, fructose, xylose, lactose, and sucrose, respectively), whereas the amino acid-derived hydrochars were denoted HC-Y (Y = Lys, Gly, Cys, GluA, and Pro for lysine, glycine, cysteine, glutamic acid, and proline, respectively).

The dried hydrochar was ground with KOH (mass ratio of 1:3) and pyrolyzed at 700 °C for 1 h under Ar flow. The product was subsequently washed with 1 M HCl, rinsed to neutral pH with deionized water and ethanol, and dried at 105 °C. The final activated carbons were named ACG-X and ACG-Y, corresponding to their hydrochar precursors. Among them, ACG represents activated coffee grounds, X represents various exogenous sugar (glucose, fructose, xylose, lactose, and sucrose), and Y represents different amino acids (lysine, glycine, cysteine, glutamic acid, and proline). A control sample, designated ACG-1-10, was prepared without any exogenous precursor under previously optimized hydrothermal-activation conditions (280 °C, 30 min)[32].

Materials characterization

Crystalline phases of the samples were identified by X-ray diffraction (XRD) using a SmartLab diffractometer (Shimadzu Corporation, Japan). The degree of graphitization and structural disorder was evaluated via Raman spectroscopy with an InVia Qontor spectrometer [AiteSi Technology (Hong Kong) Limited, China]. The pore characteristics and specific surface areas were determined from nitrogen adsorption-desorption isotherms measured at 77 K on a JW-BK 100 surface area and pore size analyzer (Beijing JWGB Sci. & Tech. Co., Ltd., China). The surface elemental composition and chemical bonding states of the materials were analyzed by X-ray photoelectron spectroscopy (XPS) utilizing an ESCALAB Xi+ spectrometer (Thermo Fisher Scientific, USA). The microstructural morphology of the samples was characterized by field-emission scanning electron microscopy (SEM) with a ZEISS Gemini SEM 500 instrument [Carl Zeiss (Shanghai) Management Co., Ltd., China]. Elemental distribution mapping was conducted by transmission electron microscopy (TEM) coupled with energy-dispersive X-ray spectroscopy (EDS) using a Talos F200X microscope [Sinopharm Scientific Equipment (Hong Kong) Co., Ltd., China]. All raw characterization data acquired from the above instruments were processed and plotted using OriginPro 2024, and all graphic combinations and layout adjustments were performed with Microsoft PowerPoint 2020.

Electrochemical characterization

Electrodes were prepared by mixing activated carbon, acetylene black, and PTFE at a mass ratio of 8:1:1. Absolute ethanol was used as the dispersing solvent, and the mixture was ultrasonically dispersed for 30 min, followed by drying at 105 °C for 6 h. Approximately 3 mg of the obtained powder was pressed into a circular pellet (diameter: 10 mm) under a pressure of 2-4 MPa, corresponding to an active material loading of approximately 3.8 $mg \cdot cm^{-2}$. The pellet was sandwiched between two nickel foams (diameter: 15 mm) to obtain the working electrode. Under the applied potential window, the electrochemical contribution of the nickel foam was negligible compared with that of the activated carbon electrode.

Electrochemical tests were carried out on a CHI 760 E workstation (Shanghai Chenhua Instrument Co., Ltd., China) in a 6 M KOH electrolyte. Cyclic voltammetry (CV) was recorded over a potential range of -1.0 V to 0 V at scan rates of 10, 20, 50, 100, and 200 $mV \cdot s^{-1}$. Galvanostatic charge-discharge (GCD) was performed at current densities of 0.5, 1, 2, 5, and 10 $A \cdot g^{-1}$. Electrochemical impedance spectroscopy (EIS) was measured from 100 kHz to 0.01 Hz with a 5 mV amplitude. All measurements were conducted at 25 ± 1 °C using N_2-purged electrolyte.

A conventional three-electrode configuration was adopted, consisting of a Hg/HgO reference electrode and a platinum plate counter electrode, with 6 M KOH as the electrolyte. The specific capacitance (C_g, $F \cdot g^{-1}$) was calculated from the GCD discharge curves according to:

$$C_g = \frac{I\Delta t}{m\Delta V} \tag{1}$$

where I is the discharge current (A), Δt is the discharge time (s), m is the active material mass (g), and ΔV is the operating potential window (V) after IR correction.

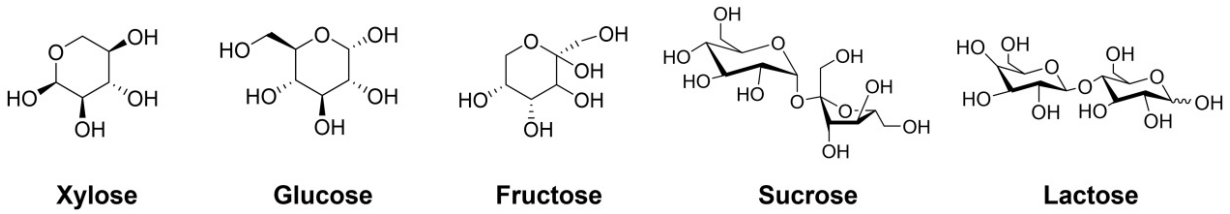

Figure 1. Molecular structures of the five sugar precursors.

For the symmetric supercapacitor assembled with two mass-matched electrodes, the device-specific capacitance (C_s, F·g^{-1}) was obtained from

$$C_s = \frac{2I\Delta t}{m\Delta V} \tag{2}$$

where I is the discharge current (A), Δt is the discharge time (s), m is the total mass of the active material on both electrodes (g), and ΔV is the cell voltage (V). The energy density (E, Wh·kg^{-1}) and power density (P, W·kg^{-1}) were determined from

$$E = \frac{C_s \Delta V^2}{8 \times 3.6} \tag{3}$$

$$P = \frac{3600E}{\Delta t} \tag{4}$$

respectively.

All the performance metrics were normalized to the total active material mass on both electrodes. All the electrochemical performance figures (such as the CV and GCD) were plotted using OriginPro 2024 on the basis of the raw data.

RESULTS AND DISCUSSION

Regulation of carbon structure and surface chemistry by sugar precursors

The molecular structures of the five selected sugars differ systematically in terms of carbon chain length (pentose *vs.* hexose), degree of polymerization (monosaccharide *vs.* disaccharide), and reducing character. These structural features govern their dehydration and condensation behavior during hydrothermal pretreatment, thereby dictating the crosslinking density of the hydrochar network and ultimately the pore architecture, defect density, and heteroatom doping configuration of the final carbon materials. The molecular structures of these sugar precursors are shown in Figure 1.

XRD analysis [Figure 2A] revealed that all the samples displayed broad diffraction peaks near 23° and 43°, indicating a predominantly amorphous carbon structure[10-12]. The (002) peak intensity varied systematically with the sugar type, with ACG-Xyl exhibiting the highest intensity, ACG-Suc the lowest, and ACG-Lac an intermediate value. As a pentose aldose, xylose possesses a shorter molecular backbone and high dehydration reactivity, enabling rapid formation of furan-rich polycondensation intermediates that promote carbon skeleton evolution along a more ordered pathway. In contrast, the nonreducing disaccharide sucrose lacks free carbonyl groups for carbonyl-amine reactions, and its glycosidic bond restricts efficient polycondensation; thus, its subsequent framework formation relies more on pyrolytic carbonization, which introduces disordered defects[22]. Lactose, although a disaccharide, contains a reducing end group and therefore strikes a balance between ordered stacking and framework openness[23].

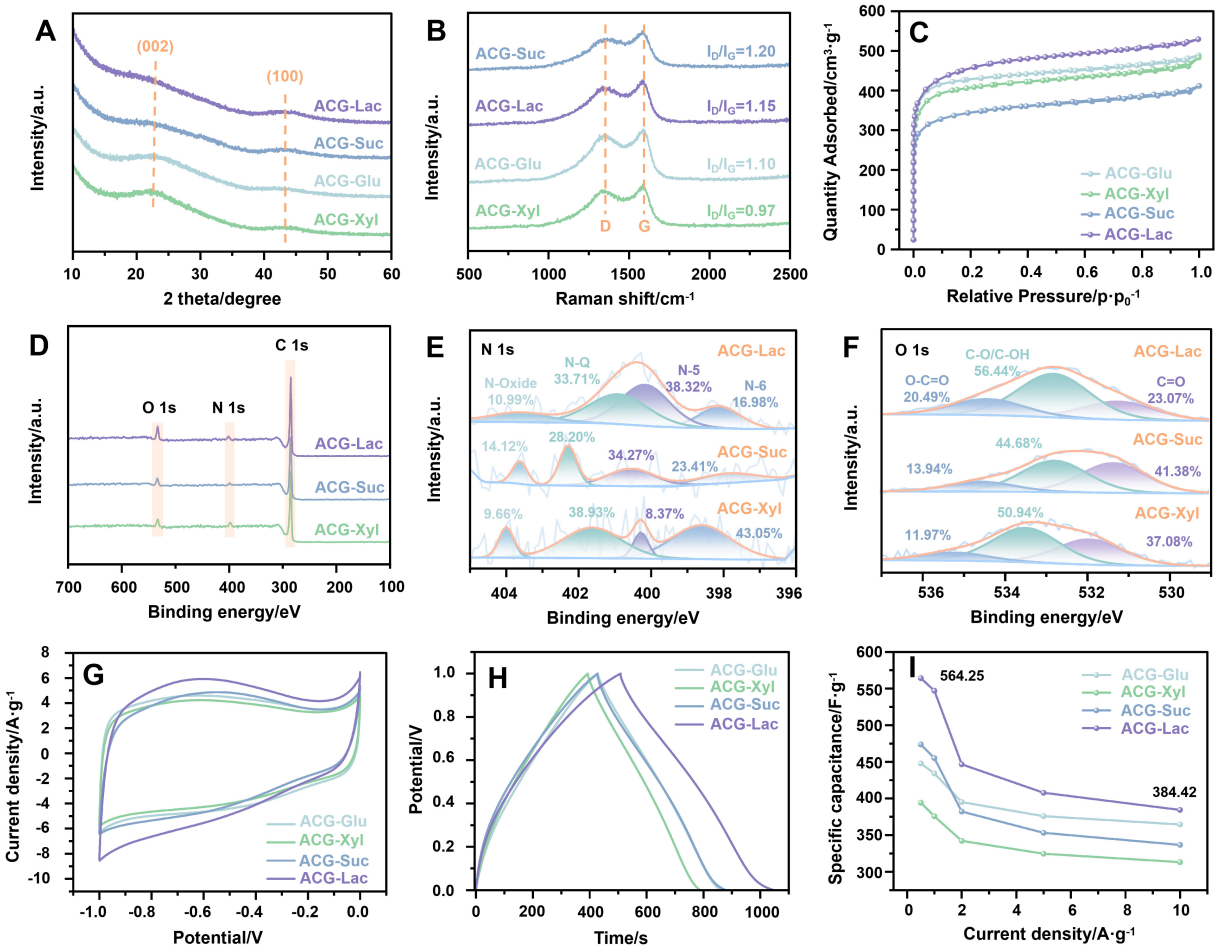

Figure 2. (A) XRD patterns, (B) Raman spectra and (C) N_2 adsorption-desorption isotherms of ACG-Glu, ACG-Xyl, ACG-Suc and ACG-Lac; (D) XPS survey spectra, (E) N 1s spectra and (F) O 1s spectra of ACG- Xyl, ACG- Suc and ACG-Lac; (G) CV curves at 10 mV·s^{-1}, (H) GCD curves at 1 A·g^{-1} and (I) Specific capacitances for ACG-Glu, ACG-Xyl, ACG-Suc and ACG-Lac electrodes. XRD: X-ray diffraction; XPS: X-ray photoelectron spectroscopy; ACG: activated coffee grounds; CV: cyclic voltammetry; GCD: galvanostatic charge-discharge.

Table 1. The I_D/I_G ratio of ACG-X (X = Xyl, Glu, Fru, Suc and Lac)

Sample	ACG-Xyl	ACG-Glu	ACG-Fru	ACG-Suc	ACG-Lac
I_D/I_G	0.97	1.10	1.12	1.20	1.15

ACG: Activated coffee grounds.

Raman spectroscopy further corroborated these trends. As shown in [Figure 2B and Table 1], the I_D/I_G ratio increased progressively from ACG-Xyl (0.97) to ACG-Suc (1.20), with ACG-Glu (1.10), ACG-Fru (1.12), and ACG-Lac (1.15) falling in between. The lowest ratio for ACG-Xyl confirms the preservation of locally ordered stacking inherited from its relatively regular polycondensation network, whereas the highest ratio for ACG-Suc reflects the abundance of disordered structures generated under pyrolysis-dominated carbonization. Although both six-carbon monosaccharides, glucose (aldose) and fructose (ketose), differ in their carbonyl position and dehydration-rearrangement pathways, resulting in a slightly higher defect density in ACG-Fru[24]. These results reinforce that the molecular structure of the sugars governs the order of polycondensations during the hydrothermal stage, which in turn dictates the degree of graphitic microcrystallite development and surface defect distribution in the final carbon.

Table 2. Detailed pore structure parameters of ACG-X (X = Xyl, Glu, Fru, Suc and Lac)

Sample	S_{BET} ($m^2 \cdot g^{-1}$)	S_{micro} ($m^2 \cdot g^{-1}$)	V_t ($cm^3 \cdot g^{-1}$)	V_{micro} ($cm^3 \cdot g^{-1}$)	D_{pores} (nm)
ACG-Xyl	1,573.38	1,423.71	0.74	0.57	1.88
ACG-Glu	1,656.39	1,518.26	0.75	0.61	1.80
ACG-Fru	1,662.64	1,522.92	0.74	0.60	1.81
ACG-Suc	1,302.03	1,127.85	0.63	0.46	1.93
ACG-Lac	1,721.70	1,510.73	0.82	0.62	1.90

ACG: Activated coffee grounds.

The N_2 adsorption-desorption isotherms and pore structure parameters of the samples are presented in Figure 2C, Supplementary Figure 1A and Table 2. All the sugar-modified samples exhibited relatively moderate specific surface areas (1,302.03-1,721.70 $m^2 \cdot g^{-1}$), indicating that the exogenous sugars enhanced hydrothermal polycondensations and led to a denser carbon framework that restricted subsequent KOH activation[25]. Among the sugar-modified samples, ACG-Glu and ACG-Fru presented the smallest average pore sizes (1.80-1.81 nm) and the highest micropore fractions (> 81%), which is consistent with the compact crosslinked networks formed from small, densely functionalized monosaccharides. The specific surface area of ACG-Xyl was lower (1,573.38 $m^2 \cdot g^{-1}$), which was attributed to its shorter five-carbon backbone and more pronounced network contraction. The specific surface area of ACG-Suc was the lowest (1,302.03 $m^2 \cdot g^{-1}$), whereas that of ACG-Lac was the greatest (1,721.70 $m^2 \cdot g^{-1}$), and the total pore volume was the greatest (0.82 $cm^3 \cdot g^{-1}$) within the group, indicating that its disaccharide backbone provides steric hindrance that mitigates excessive network contraction while retaining considerable pore accessibility after activation[33].

XPS analysis further revealed the targeted modulation of surface chemistry by the sugar precursors. All the samples displayed distinct C 1s, N 1s, and O 1s signals [Figure 2D-F and Table 3], confirming the participation of sugars in the construction of surface functional groups. Among the sugar-modified samples, ACG-Lac exhibited the highest heteroatom content (N: 1.52 at%, O: 6.12 at%), suggesting that lactose facilitates extensive carbonyl-amine reactions and achieves a high degree of N/O anchoring after carbonization. Compared with reducing sugars, ACG-Suc had the lowest nitrogen content (0.43 at%), indicating a limited nitrogen incorporation capacity[30]. N 1s fine spectra revealed distinct nitrogen configuration distributions: ACG-Xyl contained N-6 at 43.05% and N-Q at 38.93% with only 8.37% N-5, suggesting that a more ordered carbon framework favors thermally stable pyridinic N and graphitic N, which are conducive to electron transport. In contrast, ACG-Lac was dominated by N-5 (38.32%), indicating that its moderate polycondensation rate favors the preservation of edge-active nitrogen. Given that N-5 enhances pseudocapacitive activity and that N-Q improves conductivity[34], sugar precursors modulate the energy storage mechanism by regulating the nitrogen distribution. O 1s spectra revealed that ACG-Suc achieved the highest C=O proportion (41.38%, 1.77 at%) within the sugar-modified group. Although sucrose is less favorable for pore structure and nitrogen doping, its pyrolysis-driven restructuring generates abundant carbonyl groups, which enhance electrolyte wettability and contribute additional pseudocapacitance through reversible redox reactions[35]. Thus, sugar precursors establish distinct surface chemistry foundations by differentially modulating nitrogen configurations and oxygen functional groups, providing varied pseudocapacitive contributions to subsequent electrochemical processes.

The electrochemical performance of four representative sugar-derived samples is shown in [Figure 2G-I]. The CV curves at 10 $mV \cdot s^{-1}$ all exhibited quasirectangular shapes with broad redox humps, indicating that the combined electric double-layer capacitance (EDLC) and pseudocapacitive contributions[36]. The specific capacitances of all the sugar-derived activated carbons at different current densities are summarized in [Supplementary Table 1]. At 1 $A \cdot g^{-1}$, the specific capacitance followed the order ACG-Lac > ACG-Suc >

Table 3. Surface elemental composition and absolute content of active functional groups of ACG-X (X = Xyl, Glu, Fru, Suc and Lac)

Sample	C (at%)	N (at%)	O (at%)	N-5 (at%)	C=O (at%)
ACG-Xyl	95.49	0.93	3.59	0.08	1.33
ACG-Glu	95.56	0.51	3.93	0.2	0.61
ACG-Fru	95.47	0.84	3.69	0.29	1.23
ACG-Suc	95.29	0.43	4.29	0.15	1.77
ACG-Lac	92.36	1.52	6.12	0.58	1.41

ACG: Activated coffee grounds.

ACG-Fru > ACG-Glu > ACG-Xyl. The specific capacitance of ACG-Lac was 564.25 F·g^{-1} at 0.5 A·g^{-1}, which was the highest among all the sugar-modified samples. These findings demonstrate that the electrochemical performance is governed not by the surface area alone but by the synergy among the accessible pore structure, heteroatom configuration, and surface functional groups[37]. The advantage of ACG-Lac stems from three factors: the highest heteroatom content within the sugar-modified group (N + O = 7.64 at%), a higher N-5 fraction enhancing pseudocapacitance, and the highest specific surface area and total pore volume among the sugar-modified samples-together providing favorable ion transport and interfacial reaction pathways. Thus, ACG-Lac effectively compensates for pore structure loss through surface chemistry optimization. Despite having the lowest specific surface area, ACG-Suc still outperforms ACG-Xyl (473.76 *vs.* 394.26 F·g^{-1}), which is attributable to its highest C=O content in the sugar group, which provides oxygen-based pseudocapacitive sites that partially offset EDLC loss[38]. In contrast, despite having higher structural ordering and lower Rct, ACG-Xyl suffers from insufficient pore structure and active site density. These findings highlight that structural ordering alone does not guarantee high capacitance; optimal performance requires synergy among an ordered conductive network, accessible porosity, and high-density active functional groups.

The rate capability at 10 A·g^{-1} followed the order of ACG-Glu (81.4%) > ACG-Xyl (79.4%) > ACG-Fru (79.3%) > ACG-Suc (71.1%) > ACG-Lac (68.1%). The monosaccharide-derived samples, with lower functional group contents, rely more on rapid EDLC processes and thus exhibit higher rate retention, whereas the enriched N-5 and C=O sites in ACG-Lac and ACG-Suc increase the pseudocapacitive contribution but introduce more pronounced polarization at high rates. Nonetheless, ACG-Lac maintained the highest absolute capacitance among all the sugar-modified samples across 0.5-10 A·g^{-1} and outperformed all the other sugar-modified samples at 0.5 and 1 A·g^{-1}, confirming that its surface chemistry gain is most effective at low to moderate current densities. EIS analysis [Supplementary Figure 1B and Table 4] revealed comparable R_s values (0.42-0.47 Ω), whereas R_{ct} increased in the order of ACG-Glu (0.38 Ω) < ACG-Xyl (0.64 Ω) < ACG-Fru (0.66 Ω) < ACG-Lac (1.11 Ω) < ACG-Suc (1.24 Ω). The lower R_{ct} of monosaccharide-derived samples reflects their higher structural ordering, whereas the higher R_{ct} of ACG-Lac and ACG-Suc arises from the increased complexity of interfacial Faradaic processes; ACG-Suc exhibited the highest R_{ct} because of its disordered framework and dense structure. These results indicate that while a lower R_{ct} favors a rate response, surface chemistry gain plays a more decisive role in enhancing the absolute capacitance at low to moderate current densities. CV tests from 10 to 200 mV·s-1 and GCD tests [Supplementary Figure 1C and D] from 0.5 A·g^{-1} to 10 A·g^{-1} further confirmed that ACG-Lac maintains a stable CV morphology and symmetric charge-discharge profiles, demonstrating good polarization control and electrochemical reversibility[39].

In summary, the sugar precursors regulated hydrothermal polycondensations and subsequent carbonizations through three structural factors-carbon chain length, degree of polymerization, and reducing nature-enabling synergistic modulation of pore structure, structural ordering, and surface functional groups. Among

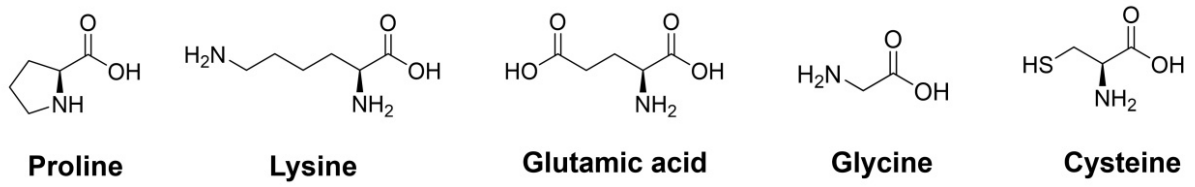

Figure 3. Molecular structures of the five amino acid precursors.

Table 4. EIS fitting equivalent circuit parameters of ACG-X (X = Xyl, Glu, Fru, Suc and Lac)

Sample	R_s (Ω)	R_{ct} (Ω)
ACG-Xyl	0.45	0.64
ACG-Glu	0.47	0.38
ACG-Fru	0.45	0.66
ACG-Suc	0.46	1.24
ACG-Lac	0.42	1.11

EIS: Electrochemical impedance spectroscopy; ACG: activated coffee grounds.

them, lactose achieved the optimal "chemical gain" owing to its moderate steric hindrance, strong surface chemistry regulation capability, and favorable pore structure retention. Despite having the poorest pore structure, sucrose obtained pronounced pseudocapacitive compensation through its high density of C=O groups. Xylose exhibited the lowest capacitive performance because of premature framework densification and insufficient active sites. These comparative results demonstrate that moderate reactivity and a suitable molecular configuration are key to minimizing pore structure loss while maximizing surface chemistry gain.

Regulation of carbon structure and surface chemistry by amino acid precursors

Unlike sugar precursors, which primarily influence the carbon framework through the modulation of dehydration-polycondensation and oxygen-containing intermediate evolution, amino acid precursors exert their regulatory effects more directly through side chain functional groups that control crosslinking modes, pyrolysis behavior, and heteroatom retention. The cyclic imino group of proline, the ε-amino group of lysine, the γ-carboxyl group of glutamic acid, the thiol group of cysteine, and the minimal backbone of glycine correspond to distinct steric hindrances, reaction site types, and heteroatom incorporation pathways, thereby enabling multidimensional regulation of defect density, pore structure parameters, and surface chemical composition. The introduction of amino acid additives thus shifts the performance optimization strategy from the passive retention of inherent N/O species in the raw material to the active manipulation of nitrogen, oxygen, and sulfur active site distribution through molecular structure design-a "chemical gain" process. The molecular structures of these amino acid precursors are shown in Figure 3.

XRD patterns [Figure 4A] revealed distinct differences in (002) peak broadening among the samples, indicating that the amino acid side chain structure directly influences the ordered stacking of carbon layers. ACG-Pro exhibited the narrowest (002) peak, suggesting the most regular local carbon layer arrangement. The rigid pyrrolidine ring in proline can serve as a conformational constraint during precursor polycondensations, guiding carbon layers toward more ordered stacking and promoting graphitic microcrystallite growth. In contrast, ACG-Cys displayed the broadest (002) peak, reflecting the highest degree of disorder. During thermal treatment, cysteine not only participates in precursor crosslinking but also introduces sulfur, which significantly alters the local electronic structure and lattice continuity of the carbon framework, thereby generating more structural distortions and edge defects[40]. Lysine, glutamic acid, and glycine each exerted distinct regulatory effects on carbon layer stacking through their straight-chain

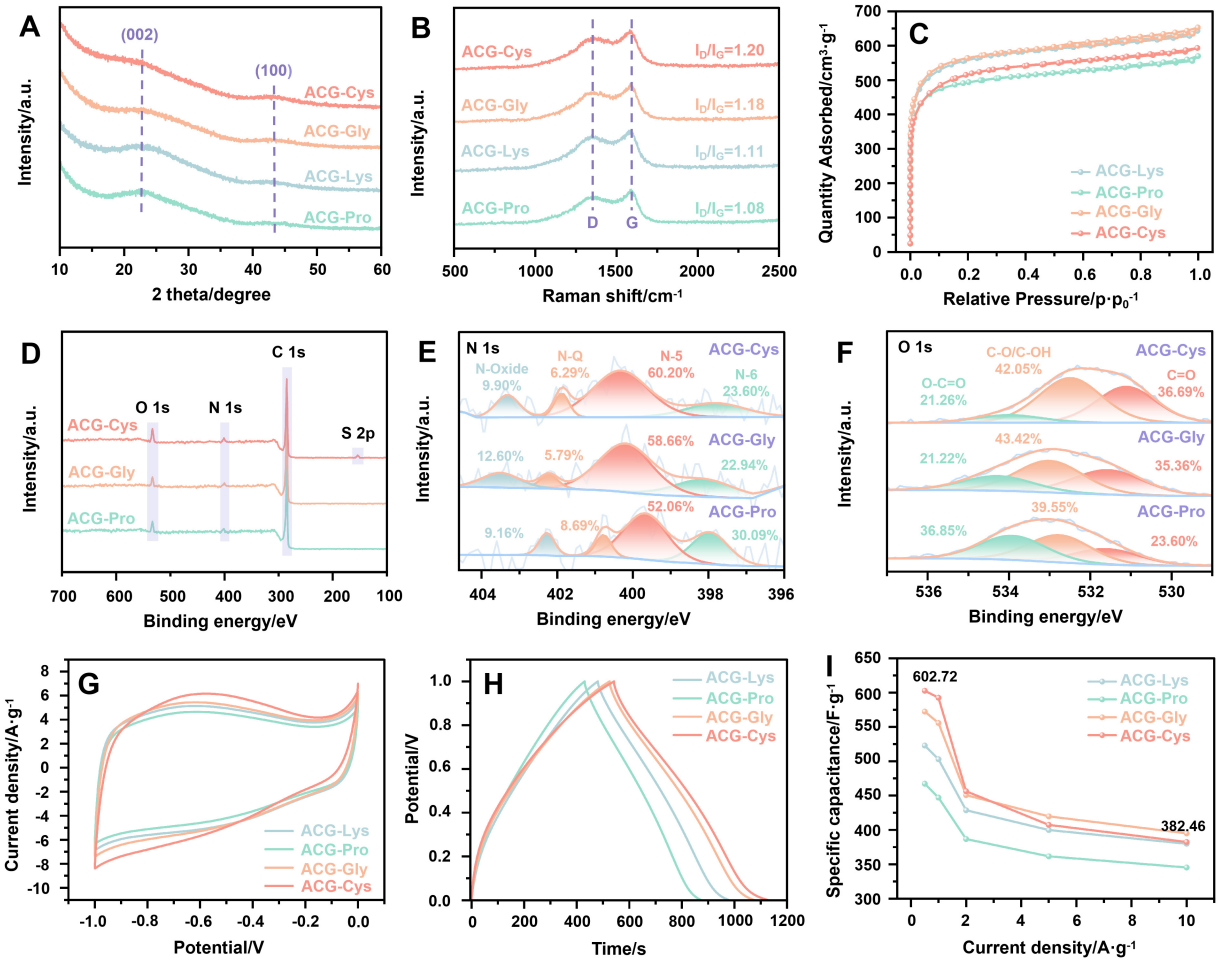

Figure 4. (A) XRD patterns, (B) Raman spectra and (C) N_2 adsorption-desorption isotherms of ACG-Lys, ACG-Pro, ACG-Gly and ACG-Cys; (D) XPS survey spectra, (E) N 1s spectra and (F) O 1s spectra of ACG-Pro, ACG-Gly and ACG-Cys; (G) CV curves at 10 mV·s^{-1}, (H) GCD curves at 1 A·g^{-1} and (I) Specific capacitance for ACG-Lys, ACG-Pro, ACG-Gly and ACG-Cys electrodes. XRD: X-ray diffraction; XPS: X-ray photoelectron spectroscopy; ACG: activated coffee grounds; CV: cyclic voltammetry; GCD: galvanostatic charge-discharge.

multifunctional groups, dicarboxyl sites, and low-steric-hindrance highly reactive backbones, respectively.

Raman spectroscopy [Figure 4B] further confirmed the modulation of defect structures by the amino acid additives. As shown in [Table 5], the I_D/I_G ratio increased in the order of ACG-Pro (1.08) < ACG-Lys (1.11) < ACG-GluA (1.16) < ACG-Gly (1.18) < ACG-Cys (1.20). The lowest ratio for ACG-Pro is consistent with the more ordered carbon stacking associated with its rigid pyrrolidine ring, suggesting that this precursor favors lower defect density. The highest ratio for ACG-Cys reflects the structural perturbation caused by sulfur incorporation: the larger covalent radius of sulfur relative to that of carbon can induce local bond length variations, thereby increasing the defect density[41]. The ratio of ACG-Lys was 1.11, which was close to that of ACG-Pro, suggesting that its straight-chain diamino structure enables crosslinking without substantially increasing structural disorder. Despite having the simplest molecular structure, glycine has a relatively high I_D/I_G of 1.18, indicating that in the absence of steric hindrance, the high reactivity of its α-amino and carboxyl groups tends to drive rapid polycondensations, generating a high density of structural defects. Overall, the amino acid side chain influences not only the type of heteroatom introduced but also the extent of framework defect formation.

Table 5. The I_D/I_G ratio of ACG-Y (Y = Pro, Lys, GluA, Gly and Cys)

Sample	ACG-Pro	ACG-Lys	ACG-GluA	ACG-Gly	ACG-Cys
I_D/I_G	1.08	1.11	1.16	1.18	1.20

ACG: Activated coffee grounds.

The hydrochar yields and activated carbon yields of the different precursor systems are summarized in Supplementary Table 2. Distinct yield variations were observed among sugars and amino acids, reflecting differences in precursor structure and hydrothermal conversion behavior. Among the sugar-derived systems, sucrose resulted in the highest hydrochar yield (46.76%), which can be attributed to its relatively low hydrothermal reactivity as a nonreducing sugar. Lactose also resulted in a relatively high hydrochar yield (41.12%), whereas the monosaccharide-derived systems resulted in lower hydrochar yields (35%-37%). With respect to amino acid-derived carbons, glycine and cysteine resulted in relatively low hydrochar yields (26.47% and 27.47%, respectively), indicating more extensive mass loss during hydrothermal treatment. Nevertheless, ACG-Cys retained a relatively high activated carbon yield (37.12%), exceeding those of the Gly-, Pro-, Lys-, and GluA-derived carbons. These results suggest that sulfur- and nitrogen-containing intermediates derived from cysteine contribute to enhanced structural stability during KOH activation, thereby suppressing excessive carbon consumption. Overall, the yield results indicate that the molecular structure of the exogenous precursor significantly influences both hydrothermal carbonization and activation processes. However, the final porous architecture results from the combined effects of precursor conversion, framework evolution, and activation behavior, as further evidenced by subsequent structural and surface chemistry characterization.

N_2 adsorption-desorption measurements [Figure 4C, Supplementary Figure 2A and Table 6] revealed the pore structure parameters of the amino acid-derived samples. All the amino acid-modified samples exhibited specific surface areas ranging from 1,737.79 to 2,153.26 $m^2 \cdot g^{-1}$, indicating that exogenous amino acids generally enhanced polycondensations during the hydrothermal stage, yielding a denser carbon framework prior to activation. The specific surface area (2,153.26 $m^2 \cdot g^{-1}$) and total pore volume (1.00 $cm^3 \cdot g^{-1}$) of ACG-Gly were the greatest among the amino acid-derived samples. This can be attributed to the minimal molecular size and simple backbone of glycine, which lacks sterically bulky or multifunctional groups that would cause premature framework densification, thereby preserving more etchable sites and diffusion channels for subsequent KOH activation[42]. ACG-Lys followed closely (2,104.41 $m^2 \cdot g^{-1}$), suggesting that the bridging structure formed by its straight-chain diamino groups enhances framework stability while maintaining reasonable structural openness[43]. The specific surface area of ACG-GluA was lower (1,894.75 $m^2 \cdot g^{-1}$); the presence of both α- and γ-carboxyl groups increased the crosslinking density during polycondensations, promoting local densification and thus limiting subsequent pore generation. The pore development of ACG-Pro was the poorest (1,737.79 $m^2 \cdot g^{-1}$), which is consistent with the close-packed carbon layer stacking induced by its rigid pyrrolidine ring-a configuration that, despite improving local ordering, significantly suppresses the formation of accessible pore volume and surface area[44]. The specific surface area of ACG-Cys was 1,920.91 $m^2 \cdot g^{-1}$; the sulfur introduced via its thiol group induced lattice distortion and local structural expansion, which partially counteracted the adverse effects of polycondensation-induced densification. All the amino acid-derived samples exhibited average pore sizes less than 2 nm, indicating that amino acid-induced crosslinking generally produces a more compact framework with a predominantly microporous character.

To further understand the influence of the precursor molecular structure on pore evolution, representative SEM images of ACG-Suc, ACG-Gly, and ACG-Cys are compared in [Figure 5A-C]. Distinct morphology differences can be observed among the three samples. The ACG-Suc sample has a relatively compact carbon

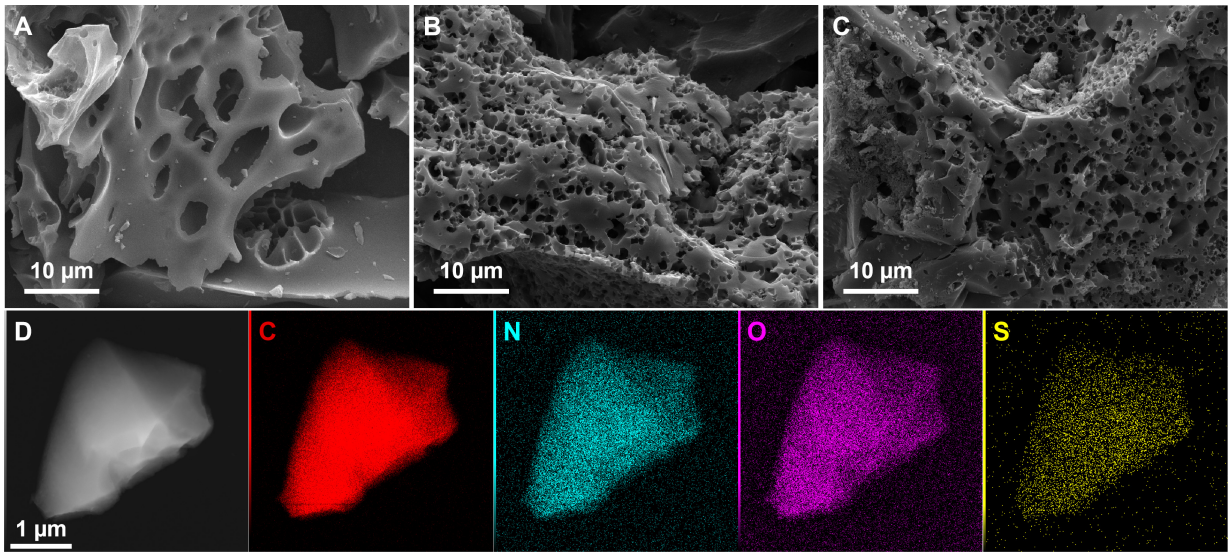

Figure 5. (A-C) SEM images of ACG-Suc, ACG-Gly, and ACG-Cys, respectively; (D) TEM image and corresponding elemental mappings of C, N, O, and S for ACG-Cys. SEM: Scanning electron microscopy; TEM: transmission electron microscopy; ACG: activated coffee grounds.

Table 6. Detailed pore structure parameters of ACG-Y (Y = Pro, Lys, GluA, Gly and Cys)

Sample	S_{BET} ($m^2 \cdot g^{-1}$)	S_{micro} ($m^2 \cdot g^{-1}$)	V_t ($cm^3 \cdot g^{-1}$)	V_{micro} ($cm^3 \cdot g^{-1}$)	D_{pores} (nm)
ACG-Pro	1,737.79	1,477.89	0.85	0.62	1.95
ACG-Lys	2,104.41	1,867.25	0.99	0.77	1.88
ACG-GluA	1,894.75	1,694.12	0.87	0.68	1.84
ACG-Gly	2,153.26	1,924.78	1.00	0.78	1.85
ACG-Cys	1,920.91	1,667.17	0.92	0.69	1.91

ACG: Activated coffee grounds.

framework with limited pore development and several large pores, which is consistent with its relatively low specific surface area and pore volume. In contrast, ACG-Gly displays a sponge-like porous network with abundant pores generated during KOH activation. ACG-Cys has a well-developed porous texture with abundant pores distributed throughout the carbon matrix while maintaining structural integrity. These observations are consistent with the BET results, indicating that the precursor molecular structure significantly influences pore formation and structural evolution during activation, thereby affecting ion transport and electrochemical charge-storage behavior. The elemental distribution of ACG-Cys was further examined by TEM. TEM elemental mapping [Figure 5D] revealed a uniform distribution of C, N, O, and S throughout the carbon framework, verifying the successful construction of an N/O/S tridoped surface.

XPS analysis further demonstrated the targeted modulation of surface chemistry by the amino acid side chain functional groups. All the samples exhibited distinct C 1s, N 1s, and O 1s signals [Figure 4D and Table 7], whereas ACG-Cys additionally displayed a clear S 2p peak, confirming successful sulfur doping and the construction of a N/O/S tri-doped surface[31]. The nitrogen content of ACG-GluA was the highest (1.23 at%), followed by that of ACG-Gly (1.19 at%), suggesting that carboxyl/amino synergy and a simple molecular backbone facilitate nitrogen retention. Notably, ACG-Lys, despite containing two amino groups, had the lowest nitrogen content (0.47 at%), indicating that the degree of doping efficiency depends on the combined effects of the side chain structure, the polycondensation pathway, and pyrolytic retention rather than the precursor nitrogen content alone[26,45]. ACG-Cys possessed the lowest carbon content (92.27 at%) and the

Table 7. Surface elemental composition and absolute content of active functional groups of ACG-Y (Y = Pro, Lys, GluA, Gly and Cys)

Sample	C (at%)	N (at%)	O (at%)	S (at%)	N-5 (at%)	C=O (at%)
ACG-Pro	95.25	0.66	4.1	-	0.34	0.97
ACG-Lys	95.85	0.47	3.68	-	0.24	1.03
ACG-GluA	93.15	1.23	5.61	-	0.62	1.85
ACG-Gly	94.55	1.19	4.26	-	0.7	1.51
ACG-Cys	92.27	1.11	6.02	0.55	0.67	2.21

ACG: Activated coffee grounds.

highest total heteroatom content (N + O + S = 7.68 at%). The N 1s fine spectra [Figure 4E] revealed that all the samples were dominated by N-5, with the proportion following the order of ACG-Cys (60.20%) > ACG-Gly (58.66%) > ACG-Pro (52.06%), all of which exhibit a high N-5 proportion (≥ 52.06%), indicating that precursors with minimal steric hindrance and well-exposed reactive sites favor the formation of edge-type pyrrolic nitrogen. The cyclic structure of proline, although conducive to ordered stacking, imposes steric constraints that partially limit edge nitrogen formation[27]. The absolute N-5 content of ACG-Gly was the highest (0.70 at%), followed by that of ACG-Cys (0.67 at%), both of which form important chemical bases for their high capacitive output.

The O 1s fine spectra [Figure 4F] revealed that ACG-Cys exhibited the highest C=O proportion (36.69%) and absolute content (2.21 at%), followed by ACG-Gly (35.36% and 1.51 at%, respectively), both of which significantly exceeded those of ACG-Pro. The high C=O content in ACG-Cys is attributed to thiol-promoted reconstruction of oxygen-containing surface sites during pyrolysis, whereas the simple backbone of glycine facilitates more complete functional group retention. The S 2p spectrum [Supplementary Figure 2B] further revealed that sulfur in ACG-Cys exists as thiophene-type sulfur (C-S-C, 57.53%) and oxidized sulfur (C-SO_x-C, 42.47%). The former enhances electron delocalization and improves the conductive network, whereas the latter provides additional Faradaic storage through redox reactions. ACG-Cys thus exemplifies the "chemical gain" mechanism: beyond increased heteroatom content, its surface chemistry optimization lies in the synergistic enhancement of active site diversity and configuration[28].

The electrochemical behavior of four representative amino acid-derived samples is shown in [Figure 4G-I], while the specific capacitances of all samples are summarized in [Supplementary Table 3]. At 1 $A \cdot g^{-1}$, the specific capacitance followed the order ACG-Cys > ACG-Gly > ACG-GluA > ACG-Lys > ACG-Pro. ACG-Cys delivered 602.72 $F \cdot g^{-1}$ at 0.5 $A \cdot g^{-1}$, which was the highest among all the samples, despite its lower specific surface area - a clear "chemical gain" driven by enriched heteroatom configurations and active functional groups[46]. Its superior performance stems from four synergistic factors: a high N-5 fraction (60.20% and 0.67 at%) providing abundant edge-active nitrogen; the highest absolute C=O content (2.21 at%) delivering strong oxygen-based pseudocapacitance; dual-function sulfur sites (0.55 at%) that enhance both the conductive network and Faradaic storage; and a still substantial surface area (1,920.91 $m^2 \cdot g^{-1}$) offering accessible interfaces for active sites. ACG-Gly, with the highest specific surface area (2,153.26 $m^2 \cdot g^{-1}$) and N-5 content (0.70 at%), and ACG-GluA, with the highest total nitrogen (1.23 at%) and considerable C=O (1.85 at%), also achieved high capacitance, whereas ACG-Pro exhibited the lowest (467.31 $F \cdot g^{-1}$), confirming that structural ordering alone is insufficient without adequate porosity and active sites. The rate capability at 10 $A \cdot g^{-1}$ followed the order of ACG-Pro (73.9%) > ACG-Lys (72.7%) > ACG-Gly (69.0%) > ACG-GluA (67.1%) > ACG-Cys (63.5%). The lower rate retention of ACG-Cys is attributed to its greater dependence on Faradaic processes at low current densities, which are inherently more susceptible to polarization at high rates[47]. EIS analysis [Supplementary Figure 2C and Table 8] revealed similar R_s values (0.46-0.48 Ω), while R_{ct} followed the order of ACG-Lys (0.94 Ω) < ACG-Gly (1.20 Ω) < ACG-Cys (1.38 Ω) < ACG-Pro (1.41 Ω) <

Table 8. EIS fitting equivalent circuit parameters of ACG-Y (Y = Pro, Lys, GluA, Gly and Cys)

Sample	R_s (Ω)	R_{ct} (Ω)
ACG-Pro	0.47	1.41
ACG-Lys	0.46	0.94
ACG-GluA	0.48	2.12
ACG-Gly	0.46	1.20
ACG-Cys	0.46	1.38

ACG: Activated coffee grounds; EIS: electrochemical impedance spectroscopy.

ACG-GluA (2.12 Ω). The lowest R_{ct} of ACG-Lys reflects its relatively high structural ordering (I_D/I_G = 1.11) and fewer pseudocapacitive sites, whereas the highest R_{ct} of ACG-GluA is attributable to dense dicarboxyl crosslinking. Although ACG-Cys exhibited a moderate R_{ct} (1.38 Ω), it still achieved the highest capacitance, confirming that the storage gain from high-density active functional groups outweighs the modest kinetic penalty[48]. The charge-storage kinetics of ACG-Cys were further analyzed using Dunn's method based on the relationship $i(v) = k_1v + k_2v^{1/2}$, where k_1v and $k_2v^{1/2}$ represent the capacitive-controlled and diffusion-controlled contributions, respectively. The capacitive-controlled contribution progressively increased from 51.36% at 10 mV s^{-1} to 87.15% at 200 mV s^{-1} [Supplementary Table 4], indicating that rapid surface-controlled charge storage became dominant at high scan rates. This enhanced pseudocapacitive behavior is attributed to the abundant N-5, C=O, and sulfur-containing functionalities in ACG-Cys, which provide additional redox-active sites and facilitate interfacial charge-transfer kinetics.

CV tests at 10-200 mV·s^{-1} and GCD tests at 0.5-10 A·g^{-1} [Supplementary Figure 2D-E] demonstrated that ACG-Cys maintains a stable CV morphology and symmetric charge-discharge profiles, indicating good electrochemical reversibility. In a symmetric supercapacitor [Figure 6A-C], ACG-Cys delivered 515.27 F·g^{-1} at 0.5 A·g^{-1}, with 66.7% retention at 10 A·g^{-1} (343.87 F·g^{-1}), confirming that its hierarchical pore structure and multiheteroatom surface chemistry remain synergistic at the device scale. The Ragone plot [Figure 6D] revealed an energy density of 17.89 Wh·kg^{-1} at 125.96 W·kg^{-1}, retaining 11.94 Wh·kg^{-1} at 2,438.03 W·kg^{-1}, surpassing most reported biomass-derived porous carbons for symmetric supercapacitors in aqueous electrolytes[49-56]. A detailed comparison of the key performance metrics, including the electrolyte, voltage window, specific capacitance, energy density, and power density, is summarized in [Supplementary Table 5] [Supplementary Materials]. Long-term cycling tests [Figure 6E] revealed a capacitance retention of 76.35% after 15,000 cycles, with the Coulombic efficiency stably maintained between 99.5% and 100.5%, demonstrating acceptable cycling stability and reversible charge-storage behavior over prolonged cycling.

CONCLUSION

This study systematically investigated the regulatory effects of sugar and amino acid precursors on the pore structure, carbon framework ordering, heteroatom configuration, and electrochemical performance of ground-derived porous carbons in coffee, elucidating the "chemical gain" mechanism by which surface chemistry optimization compensates for physical charge storage loss. Among the sugar precursors, lactose achieved the optimal balance between pore retention and heteroatom enrichment (N: 1.52 at%, O: 6.12 at%), delivering 564.25 F·g^{-1} at 0.5 A·g^{-1}, while sucrose obtained pseudocapacitive compensation via high C=O content despite having the lowest surface area, and xylose experienced premature densification. Among the amino acid precursors, cysteine achieved N/O/S tri-doping with the highest N-5, C=O, and functional sulfur sites, achieving the highest capacitance (602.72 F·g^{-1}) and an energy density of 17.89 Wh·kg^{-1}; glycine excelled through its high surface area and N-5 content, while proline was limited by excessive framework densification despite ordered stacking. These results demonstrate that moderate precursor reactivity, a suitable molecular configuration, and efficient heteroatom anchoring are key to maximizing surface

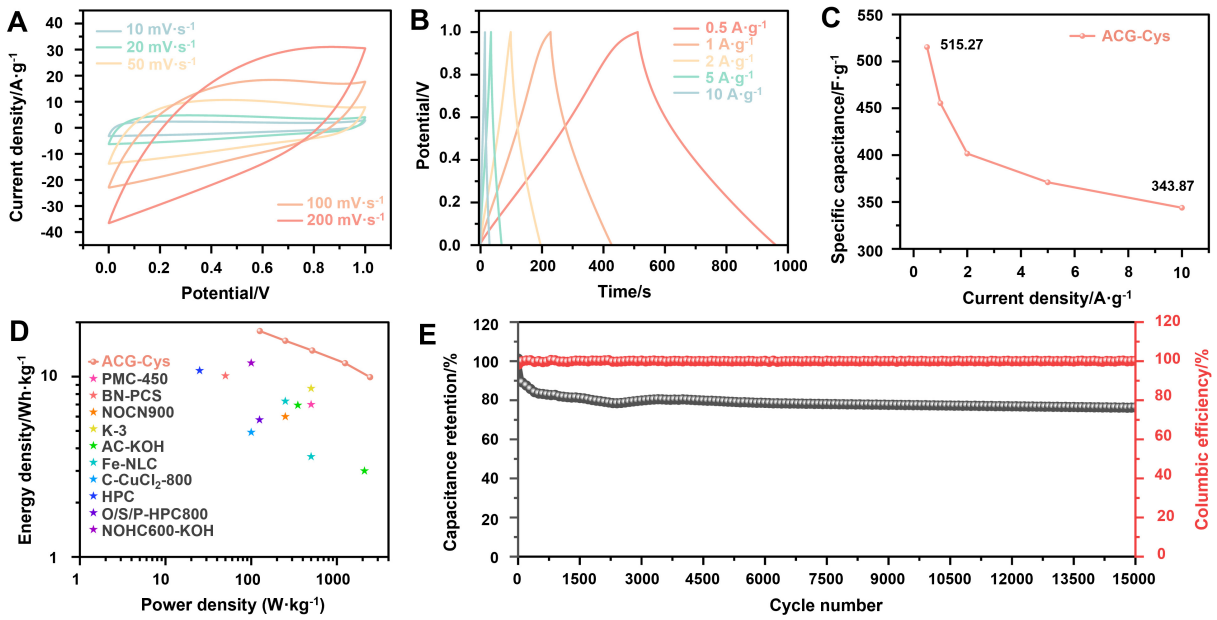

Figure 6. (A) CV curves at various scan rates, (B) GCD curves at various current densities, (C) Specific capacitance and (D) Ragone plot for ACG-Cys SSC; (E) Cycling stability performance at 10 A·g^{-1}. CV: Cyclic voltammetry; GCD: galvanostatic charge-discharge; ACG: activated coffee grounds; SSC: symmetric supercapacitor.

chemistry gain while minimizing pore structure loss, providing a rational design principle for high-performance biomass-derived porous carbon electrodes.

DECLARATIONS

Authors' contributions

Writing - original draft, visualization, validation, methodology, investigation, formal analysis, data curation, conceptualization: Du, Y.

Investigation: Yang, Y.

Supervision, funding acquisition, project administration, review and editing: Duan, P.

Availability of data and materials

The original contributions presented in this study are included in the article and Supplementary Materials. Further inquiries can be directed to the corresponding authors.

AI and AI-assisted tools statement

During the preparation of this manuscript, the AI tool OpenAI (version OpenAI, released 2026-04-24) was used solely for language editing. The tool did not influence the study design, data collection, analysis, interpretation, or the scientific content of the work. All authors take full responsibility for the accuracy, integrity, and final content of the manuscript.

Financial support and sponsorship

This study was supported by the National Key Research and Development Program of China (2024YFE0101800) and the National Natural Science Foundation of China (52370150).

Conflicts of interest

All authors declared that there are no conflicts of interest.

Ethical approval and consent to participate

Not applicable.

Consent for publication

Not applicable.

Copyright

© The Author(s) 2026.

Supplementary Materials

Supplementary Materials

REFERENCES

1. Yang, X.; Lv, T.; Qiu, J. High mass-loading biomass-based porous carbon electrodes for supercapacitors: review and perspectives. *Small* **2023**, *19*, e2300336. DOI PubMed
2. Salanne, M.; Rotenberg, B.; Naoi, K.; et al. Efficient storage mechanisms for building better supercapacitors. *Nat. Energy.* **2016**, *1*, 16070. DOI
3. Shao, Y.; El-Kady, M. F.; Sun, J.; et al. Design and mechanisms of asymmetric supercapacitors. *Chem. Rev.* **2018**, *118*, 9233-80. DOI
4. Simon, P.; Gogotsi, Y. Perspectives for electrochemical capacitors and related devices. *Nat. Mater.* **2020**, *19*, 1151-63. DOI PubMed
5. Guo, Z.; Han, X.; Zhang, C.; et al. Activation of biomass-derived porous carbon for supercapacitors: a review. *Chin. Chem. Lett.* **2024**, *35*, 109007. DOI
6. Wang, Y.; Zhang, L.; Hou, H.; et al. Recent progress in carbon-based materials for supercapacitor electrodes: a review. *J. Mater. Sci.* **2021**, *56*, 173-200. DOI
7. Adan-Mas, A.; Alcaraz, L.; Arévalo-Cid, P.; López-Gómez, F. A.; Montemor, F. Coffee-derived activated carbon from second biowaste for supercapacitor applications. *Waste. Manag.* **2021**, *120*, 280-9. DOI PubMed
8. Ramasahayam, S. K.; Clark, A. L.; Hicks, Z.; Viswanathan, T. Spent coffee grounds derived P, N co-doped C as electrocatalyst for supercapacitor applications. *Electrochim. Acta.* **2015**, *168*, 414-22. DOI
9. Ballesteros, L. F.; Teixeira, J. A.; Mussatto, S. I. Chemical, functional, and structural properties of spent coffee grounds and coffee silverskin. *Food. Bioprocess. Technol.* **2014**, *7*, 3493-503. DOI
10. Cao, K. L. A.; Kitamoto, Y.; Iskandar, F.; Ogi, T. Sustainable porous hollow carbon spheres with high specific surface area derived from Kraft lignin. *Adv. Powder. Technol.* **2021**, *32*, 2064-73. DOI
11. Chen, Y.; Wang, Z.; Mei, X.; Wang, Q.; Xie, H.; Li, Y. Nitrogen and oxygen-codoped dense porous carbon enhancing ion adsorption for high-volumetric performance supercapacitors. *Energy. Mater.* **2025**, *5*, 500146. DOI
12. Li, W.; Zhang, W.; Xu, Y.; et al. Heteroatom-doped lignin derived carbon materials with improved electrochemical performance for advanced supercapacitors. *Chem. Eng. J.* **2024**, *497*, 154829. DOI
13. Wang, J.; Kaskel, S. KOH activation of carbon-based materials for energy storage. *J. Mater. Chem.* **2012**, *22*, 23710. DOI
14. Zhang, S.; Yu, Y.; Xie, M.; et al. Clean production of N, O-doped activated carbon by water vapor carbonization/activation of expired coffee for high-volumetric supercapacitor. *Appl. Surf. Sci.* **2022**, *589*, 153011. DOI
15. Hsieh, T.; Wang, H.; Yu, G.; Huang, G.; Lin, J. Meso-pore dominant activated carbon from spent coffee grounds for high-performance electrochemical capacitors in organic electrolyte. *J. Environ. Chem. Eng.* **2021**, *9*, 106418. DOI
16. Liu, H.; Zhu, S.; Zhang, Y.; et al. Unveiling superior capacitive behaviors of one-pot molten salt-engineered B, N Co-doped porous carbon sheets. *Small* **2023**, *19*, e2204119. DOI
17. Wang, C.; Wu, D.; Wang, H.; Gao, Z.; Xu, F.; Jiang, K. Biomass derived nitrogen-doped hierarchical porous carbon sheets for supercapacitors with high performance. *J. Colloid. Interface. Sci.* **2018**, *523*, 133-43. DOI
18. Qiao, J.; Wang, Z.; Gao, Y.; Zhou, W.; Han, M.; Wei, F. The influence of heteroatoms on the properties and supercapacitive performance of carbon materials: a review. *J. Energy. Storage.* **2025**, *140*, 119016. DOI
19. Taer, E.; Apriwandi, A.; Taslim, R. Heteroatom-doped biomass-derived porous carbon for supercapacitor applications: a review. *Trends. Sci.* **2025**, *22*, 10115. DOI
20. Djandja, O. S.; Yin, L.; Wang, Z.; Duan, P.; Xu, D.; Kapusta, K. Synthesis of N-doped carbon material via hydrothermal carbonization: Effects of reaction solvent and nitrogen source. *J. Energy. Storage.* **2023**, *60*, 106588. DOI
21. Djandja, O. S.; Liew, R. K.; Liu, C.; et al. Catalytic hydrothermal carbonization of wet organic solid waste: a review. *Sci. Total. Environ.* **2023**, *873*, 162119. DOI
22. Zhao, Y.; Zhao, Y.; Zheng, J.; et al. Designing spherical sucrose-derived hard carbon materials with abundant closed pores via amino-aldehyde condensation. *Energy. Fuels.* **2025**, *39*, 5974-85. DOI
23. Myronyuk, I. F.; Mandzyuk, V. I.; Sachko, V. M.; Gun'ko, V. M. Structural features of carbons produced using glucose, lactose, and saccharose. *Nanoscale. Res. Lett.* **2016**, *11*, 508. DOI PubMed PMC

24. Shi, N.; Liu, Q.; He, X.; et al. Molecular structure and formation mechanism of hydrochar from hydrothermal carbonization of carbohydrates. *Energy. Fuels.* **2019**, *33*, 9904-15. DOI
25. Inkoua, S.; Li, C.; Shao, Y.; et al. Co-hydrothermal carbonization of fruit peel with sugars or furfural impacts structural evolution of hydrochar. *Ind. Crops. Prod.* **2023**, *193*, 116221. DOI
26. Gao, X.; Chen, Z.; Yao, Y.; et al. Direct heating amino acids with silica: a universal solvent-free assembly approach to highly nitrogen-doped mesoporous carbon materials. *Adv. Funct. Mater.* **2016**, *26*, 6649-61. DOI
27. Yang, Z.; Xing, G.; Hou, P.; Han, D. Amino acid-mediated N-doped graphene aerogels and its electrochemical properties. *Mater. Sci. Eng. B.* **2018**, *228*, 198-205. DOI
28. Hong, J.; Kim, H.; Lee, J. E.; et al. Nitrogen and sulfur dual-doped porous carbon derived from coffee waste and cysteine for electrochemical energy storage. *Korean. J. Chem. Eng.* **2020**, *37*, 1218-25. DOI
29. Wang, Q.; Xu, Q.; Du, Z.; Zhang, W.; Wang, D.; Peng, Y. Mechanistic insights into the effects of biopolymer conversion on macroscopic physical properties of waste activated sludge during hydrothermal treatment: importance of the Maillard reaction. *Sci. Total. Environ.* **2021**, *769*, 144798. DOI
30. Mainali, K.; Garcia-perez, M. Effect of H_3PO_4 and NaOH additives on the Co-carbonization of cellulose and N-containing compounds to produce N-doped chars. *J. Anal. Appl. Pyrolysis.* **2023**, *169*, 105837. DOI
31. Kim, C. K.; Choi, I. T.; Kang, S. H.; Kim, H. K. Anchovy-derived nitrogen and sulfur co-doped porous carbon materials for high-performance supercapacitors and dye-sensitized solar cells. *RSC. Adv.* **2017**, *7*, 35565-74. DOI
32. Du, Y.; Cao, C.; Chen, L.; Jiang, Z.; Duan, P. Engineered N/O-doped hierarchical porous carbons from coffee grounds for high-performance supercapacitors. *Chem. Eng. J.* **2025**, *526*, 170934. DOI
33. Yu, L.; Falco, C.; Weber, J.; White, R. J.; Howe, J. Y.; Titirici, M. M. Carbohydrate-derived hydrothermal carbons: a thorough characterization study. *Langmuir* **2012**, *28*, 12373-83. DOI PubMed
34. Zheng, Y.; Chen, K.; Jiang, K.; Zhang, F.; Zhu, G.; Xu, H. Progress of synthetic strategies and properties of heteroatoms-doped (N, P, S, O) carbon materials for supercapacitors. *J. Energy. Storage.* **2022**, *56*, 105995. DOI
35. Cui, Z.; Liu, H.; An, X.; An, X.; Qiao, Z.; Wang, Y. Synergistic regulation of carbonyl oxygen active sites and micropores in lignite-derived porous carbon for high-performance supercapacitors. *J. Electroanal. Chem.* **2025**, *997*, 119488. DOI
36. Borenstein, A.; Hanna, O.; Attias, R.; Luski, S.; Brousse, T.; Aurbach, D. Carbon-based composite materials for supercapacitor electrodes: a review. *J. Mater. Chem. A.* **2017**, *5*, 12653-72. DOI
37. Wang, J.; Huo, T.; Zhao, Y.; Lu, R.; Wu, X. Recent advances in heteroatoms-doped porous carbon electrode materials for supercapacitors: a review. *J. Energy. Storage.* **2025**, *110*, 115216. DOI
38. Zhai, Z.; Zhang, L.; Du, T.; et al. A review of carbon materials for supercapacitors. *Mater. Design.* **2022**, *221*, 111017. DOI
39. Fleischmann, S.; Mitchell, J. B.; Wang, R.; et al. Pseudocapacitance: from fundamental understanding to high power energy storage materials. *Chem. Rev.* **2020**, *120*, 6738-82. DOI
40. Mishra, R.; Panda, P.; Barman, S. Synthesis of sulfur-doped porous carbon for supercapacitor and gas adsorption applications. *Int. J. Energy. Res.* **2022**, *46*, 2585-600. DOI
41. Kiciński, W.; Szala, M.; Bystrzejewski, M. Sulfur-doped porous carbons: synthesis and applications. *Carbon* **2014**, *68*, 1-32. DOI
42. Shao, Y.; Hu, Z.; Yao, Y.; Wei, X.; Gao, X.; Wu, Z. Glycine-derived nitrogen-doped ordered mesoporous carbons with a bimodal mesopore size distribution for supercapacitors and oxygen reduction. *Carbon* **2022**, *192*, 485-6. DOI
43. Wan, X.; Li, Y.; Xiao, H.; Pan, Y.; Liu, J. Hydrothermal synthesis of nitrogen-doped ordered mesoporous carbon via lysine-assisted self-assembly for efficient CO_2 capture. *RSC. Adv.* **2020**, *10*, 2932-41. DOI
44. Zhang, J.; Qi, L.; Zhu, X.; et al. Proline-derived in situ synthesis of nitrogen-doped porous carbon nanosheets with encaged Fe_2O_3@Fe_3C nanoparticles for lithium-ion battery anodes. *Nano. Res.* **2017**, *10*, 3164-77. DOI
45. Liang, X.; Peng, S.; Lei, Y.; et al. Effect of l-glutamic acid on the positive electrolyte for all-vanadium redox flow battery. *Electrochim. Acta.* **2013**, *95*, 80-6. DOI
46. Zhao, C.; Han, S.; Ding, Y.; Yang, Y.; Jiang, R.; Zhao, C. One-step synthesis of amino acid-derived HTC/NiO/$Ni(OH)_2$@Ni cathode for high performance supercapacitors. *Appl. Surf. Sci.* **2021**, *558*, 149853. DOI
47. Huang, Z. H.; Liu, T. Y.; Song, Y.; Li, Y.; Liu, X. X. Balancing the electrical double layer capacitance and pseudocapacitance of hetero-atom doped carbon. *Nanoscale* **2017**, *9*, 13119-27. DOI
48. Hrubiak, A.; Beyene, A.; Gogitidze, Z.; Kieush, L.; Yastremska, H.; Homenuk, I. Structural arrangement, electroconductivical and electrochemical behaviours of solid amino acid-based electrodes. *J. Electroanal. Chem.* **2024**, *970*, 118526. DOI
49. Zhang, H.; Sun, X.; Zheng, Y.; Zhou, J. Scalable synthesis of N, O co-doped hierarchical porous carbon for high energy density supercapacitors. *J. Colloid. Interface. Sci.* **2024**, *658*, 1025-34. DOI

50. Gadipelli, S.; Howard, C. A.; Guo, J.; et al. Superior multifunctional activity of nanoporous carbons with widely tunable porosity: enhanced storage capacities for carbon-dioxide, hydrogen, water, and electric charge. *Adv. Energy. Mater.* **2020**, *10*, 1903649. DOI
51. Wang, Y.; Xia, Y.; Dong, X.; Qiao, P.; Wang, W.; Song, H. Enhanced electrochemical performance of K_2CO_3-activated porous carbons from chitosan and cellulose for supercapacitor applications. *Mater. Today. Commun.* **2025**, *48*, 113327. DOI
52. Wang, J.; Qin, F.; Guo, Z.; Shen, W. Oxygen- and nitrogen-enriched honeycomb-like porous carbon from *laminaria japonica* with excellent supercapacitor performance in aqueous solution. *ACS. Sustainable. Chem. Eng.* **2019**, *7*, 11550-63. DOI
53. Chiu, Y.; Lin, L. Effect of activating agents for producing activated carbon using a facile one-step synthesis with waste coffee grounds for symmetric supercapacitors. *J. Taiwan. Inst. Chem. Eng.* **2019**, *101*, 177-85. DOI
54. Li, W.; Li, C.; Xu, Y.; et al. Heteroatom-doped and graphitization-enhanced lignin-derived hierarchically porous carbon via facile assembly of lignin-Fe coordination for high-voltage symmetric supercapacitors. *J. Colloid. Interface. Sci.* **2024**, *659*, 374-84. DOI
55. Zheng, L.; Tang, B.; Dai, X.; et al. High-yield synthesis of N-rich polymer-derived porous carbon with nanorod-like structure and ultrahigh N-doped content for high-performance supercapacitors. *Chem. Eng. J.* **2020**, *399*, 125671. DOI
56. Li, L.; Hu, X.; Guo, N.; Chen, S.; Yu, Y.; Yang, C. Synthesis O/S/N doped hierarchical porous carbons from kelp via two-step carbonization for high rate performance supercapacitor. *J. Mater. Res. Technol.* **2021**, *15*, 6918-28. DOI

Disclaimer/Publisher's Note: All statements, opinions, and data contained in this publication are solely those of the individual author(s) and contributor(s) and do not necessarily reflect those of OAE and/or the editor(s). OAE and/or the editor(s) disclaim any responsibility for harm to persons or property resulting from the use of any ideas, methods, instructions, or products mentioned in the content.

© The Author(s) 2026. Open Access This article is licensed under a Creative Commons Attribution 4.0 International License (https://creativecommons.org/licenses/by/4.0/), which permits unrestricted use, sharing, adaptation, distribution and reproduction in any medium or format, for any purpose, even commercially, as long as you give appropriate credit to the original author(s) and the source, provide a link to the Creative Commons license, and indicate if changes were made.